

Achieving Submicrometer Spatial Resolution for Neutron Imaging With Nuclear Emulsion

Abdul Muneem (✉ abdul.muneem@riken.jp)

RIKEN

Junya Yoshida

RIKEN

Hiroyuki Ekawa

RIKEN

Masahiro Hino

Kyoto University

Katsuya Hirota

High Energy Accelerator Research Organization

Go Ichikawa

High Energy Accelerator Research Organization

Ayumi Kasagi

RIKEN

Masaaki Kitaguchi

Nagoya University

Naoto Muto

Nagoya University

Kenji Mishima

High Energy Accelerator Research Organization

Jameel Nabi

University of Wah

Manami Nakagawa

RIKEN

Naotaka Naganawa

Nagoya University

Takehiko Saito

RIKEN

Research Article

Keywords: submicrometer, neutron, nuclear emulsion

Posted Date: October 21st, 2021

DOI: <https://doi.org/10.21203/rs.3.rs-966133/v1>

License:  This work is licensed under a Creative Commons Attribution 4.0 International License.

[Read Full License](#)

1 Achieving submicrometer spatial resolution for 2 neutron imaging with nuclear emulsion

3 Abdul Muneem^{1,2,*}, Junya Yoshida^{1,3,*}, Hiroyuki Ekawa¹, Masahiro Hino⁴, Katsuya
4 Hirota⁵, Go Ichikawa^{5,6}, Ayumi Kasagi^{1,7}, Masaaki Kitaguchi^{8,9}, Naoto Muto⁸, Kenji
5 Mishima^{5,6}, Jameel-Un Nabi^{2,10}, Manami Nakagawa¹, Naotaka Naganawa^{8,11}, and
6 Takehiko R. Saito^{1,12,13,*}

7 ¹High Energy Nuclear Physics Laboratory, Cluster for Pioneering Research, RIKEN, Wako, Saitama, Japan

8 ²Faculty of Engineering Sciences, GIK Institute of Engineering Sciences and Technology, KP, Pakistan

9 ³Department of Physics, Tohoku University, Sendai, Japan

10 ⁴Institute for Integrated Radiation and Nuclear Science, Kyoto University, Kumatori, Osaka, Japan

11 ⁵High Energy Accelerator Research Organization(KEK), Tsukuba, Ibaraki, Japan

12 ⁶J-PARC Center, Tokai, Ibaraki, Japan

13 ⁷Graduate School of Engineering, Gifu University, Gifu, Japan

14 ⁸Department of Physics, Nagoya University, Nagoya, Japan

15 ⁹Kobayashi-Maskawa Institute for Origin of Particles and the Universe (KMI), Nagoya University, Nagoya, Japan

16 ¹⁰University of Wah, Wah Cantt, Punjab, Pakistan

17 ¹¹Institute of Materials and Systems for Sustainability, Nagoya University, Nagoya, Japan

18 ¹²GSI Helmholtz Centre for Heavy Ion Research, Planckstrasse, Darmstadt, Germany

19 ¹³School of Nuclear Science and Technology, Lanzhou University, Lanzhou, China

20 *abdul.muneem@riken.jp

21 *junya.yoshida@a.riken.jp

22 *takehiko.saito@riken.jp

23 ABSTRACT

Neutron imaging is a non-destructive inspection technique with a wide range of potential applications. One of the key technical interests concerning neutron imaging is to achieve micrometer-scale spatial resolution. However, developing a neutron detector with a high spatial resolution is a challenging task. Recent efforts are focused on achieving this milestone or even submicrometer spatial resolution. Herein, we introduce our technique for neutron imaging using a fine-grained nuclear emulsion and evaluate the spatial resolution. We used the fine-grained nuclear emulsion with a gadolinium-based Siemens star test pattern and a grating with a periodic structure of 9 μm . The deduced value of the spatial resolution is less than 1 μm using the developed technique. To the best of our knowledge, the submicrometer spatial resolution that we achieved using our method is the best among all reported neutron imaging devices.

25 Introduction

26 Neutron beams are unique tools for a wide range of applications¹⁻⁵. Neutrons have no electrical charge and can interact directly
27 with subatomic nuclei. The absorption and scattering cross-sections of neutrons depend on the nuclides. For example, hydrogen,
28 lithium, and gadolinium exhibit high attenuations of the incident neutron beam; however, low attenuations are observed for
29 aluminum, silicon, and lead. This dependence of the attenuation of neutrons is different from that of X-rays which is correlated
30 to the atomic number⁶. Therefore, neutron imaging is an effective method for non-destructive and non-invasive observation
31 to visualise the distribution of elements using the difference in their neutron attenuation coefficients¹. The major challenges
32 in developing neutron imaging techniques include improvements in spatial resolution⁷⁻¹³, detection efficiency⁷, and time
33 resolution^{4,14} of neutron detectors. In particular, recent developments have improved the spatial resolution of neutron imaging
34 to a few micrometers⁷⁻¹³. The highest resolution currently reported is 2 μm , which has been achieved using gadolinium
35 oxysulfide scintillators and dedicated optics¹⁵. However, achieving a spatial resolution of less than 1 μm remains a challenge.

36 To achieve a submicrometer spatial resolution for neutron imaging, a nuclear emulsion is a potential candidate for a neutron
37 detector. A nuclear emulsion is a photographic film that can detect the three-dimensional trajectories of charged particles.
38 Nuclear emulsions were initially developed for particle and nuclear physics experiments to observe the tracks of charged

39 particles. They were used to make the first observations of pion¹⁶, hypernuclei^{17,18}, charm particles¹⁹, and double strangeness
40 hypernuclei²⁰ until 1970s. The analysis speed of nuclear emulsions has increased remarkably with improvements in image
41 processing techniques^{21,22}. These improvements enable the use of nuclear emulsion in modern experiments to study tau
42 neutrino interactions²³, direct observation of neutrino oscillations²⁴, hypernuclei^{22,25-28}, and for several other applications
43 including muon radiography^{29,30}.

44 Since the last decade, it has become possible to produce dedicated nuclear emulsions for specific purposes by controlling
45 the grain size of the silver halide crystals and chemical components to achieve optimal spatial resolution and sensitivity.
46 Fine-grained nuclear emulsions with silver halide crystals having a diameter of less than 0.1 μm have been developed³¹⁻³³ to
47 detect the tracks of the nuclei recoiled by the so-called weakly interacting massive particles. The sensitivity of the nuclear
48 emulsion was optimised to track the nuclei but was maintained sufficiently low for electrons and γ -rays³⁴. This type of
49 fine-grained nuclear emulsion can be used for neutron imaging by combining it with the $^{10}\text{B}_4\text{C}$ thin layer, which absorbs
50 neutrons and emits charged particles heading in the opposite direction via the following process: $^{10}\text{B} + \text{n} \rightarrow ^7\text{Li} + ^4\text{He}$. When
51 a charged particle passes through an emulsion layer, latent image specks are created in some silver halide crystals along its
52 trajectory. After chemical development, each crystal which contain latent image specks changes to an enlarged silver grain. A
53 series of these grains indicates the tracks of the charged particles.

54 Naganawa et al. reported that the spatial resolution of a neutron absorption point is less than 0.1 μm by using a fine-grained
55 nuclear emulsion under the condition that the track density within ten tracks per $(100 \mu\text{m})^2$ in Refs.³⁵. However, to apply this
56 detector to neutron imaging, the accumulated track density must be several orders of magnitude higher than the track density.
57 For example, while determining the neutron transmission rate of an area of $(10 \mu\text{m})^2$ at an accuracy of 1% compared to the
58 surrounding area, the magnitude of the track density should be 10^6 per $(100 \mu\text{m})^2$ to reduce the statistical error. The recorded
59 tracks get severely overlapped at such a high track density condition. Hence, it becomes difficult to use an analysis method
60 for individual tracks. Hirota et al. attempted neutron imaging under a high track density condition using fine-grained nuclear
61 emulsion³⁶. They succeeded in visualizing the inner components of a crystal oscillator chip, for example, gold wires with a
62 diameter of approximately 30 μm . However, the spatial resolution was not evaluated quantitatively. Therefore, it is important
63 to conduct a quantitative analysis of the spatial resolution of this neutron imaging technique with an object having well-defined
64 micrometer-scale structure.

65 In this study, we developed a new technique for neutron imaging using a fine-grained nuclear emulsion. We attempted
66 neutron imaging using the developed technique for the Siemens star test pattern and the gadolinium-based grating with a
67 periodic structure of 9 μm . The spatial resolution of neutron imaging was quantitatively deduced using the gadolinium-based
68 grating.

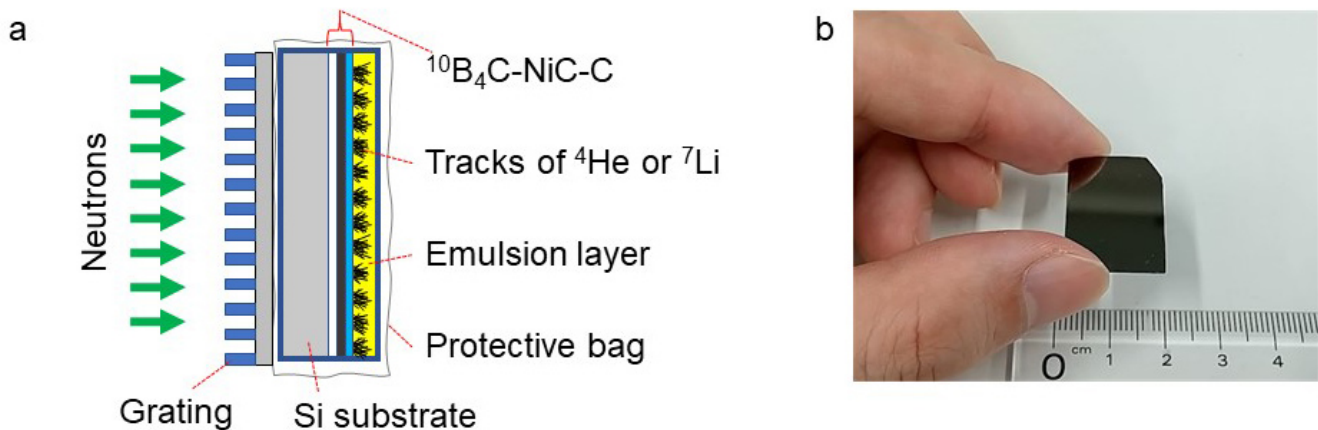


Figure 1. Developed neutron detector with the nuclear emulsion. **a** Schematic layout of the neutron detector using a fine-grained emulsion packed in a protective bag combined with a gadolinium-based grating. **b** Photograph of developed neutron detector. The size of the detector was 25 mm \times 15 mm.

69 Results

70 Neutron detector system using a fine-grained nuclear emulsion

71 The neutron detector used in this study has a layered structure, as shown in Figure 1a. The base of the detector is a 0.4 mm-thick
72 silicon substrate. On this substrate, $^{10}\text{B}_4\text{C}$, NiC, and C layers of thickness 0.23 μm , 46 nm, and 14 nm, respectively, were

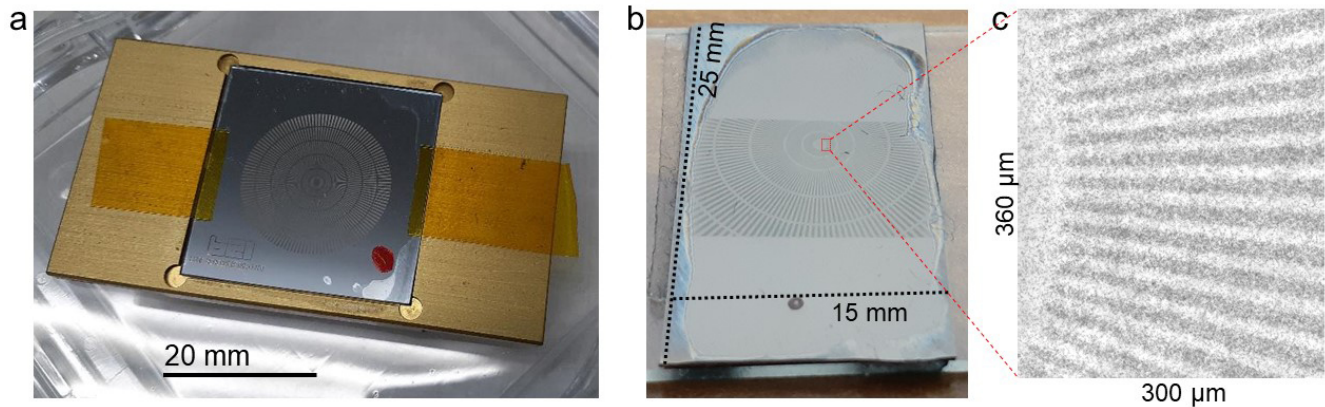


Figure 2. Neutron imaging of the Siemens star test pattern. **a** Photograph of the Siemens star test pattern. It consists of a thin layer of gadolinium on a quartz substrate and is housed in an aluminum frame. **b** Photograph of the developed detector irradiated with the neutron beam through the pattern. The pattern is visible on the emulsion layer to the eyes. **c** Micrograph of the recorded image pattern in the nuclear emulsion, showing the innermost edge of the pattern. The sizes of the vertical and horizontal directions of the figure correspond to 360 and 300 μm , respectively, as shown in the figure.

73 formed by using an ion beam sputtering technique³⁷. The $^{10}\text{B}_4\text{C}$ layer converts an incident neutron into two charged particles,
 74 ^4He and ^7Li . The NiC layer is used to physically stabilise the $^{10}\text{B}_4\text{C}$ layer. The C layer was used for chemical protection from
 75 the NiC layer and for providing a strong adhesion to the emulsion. An emulsion layer of thickness of 10 μm was formed on the
 76 sputtered layers. It is composed of silver halide crystals of approximately 40 nm diameter dispersed in gelatin and including
 77 polyvinyl alcohol.

78 During the beam exposure, the neutron detector, and the grating were placed close together to minimise the blurring
 79 effects induced by the spreading of the transmitted neutron beam, as shown in Figure 1a. A portion of the incident neutrons
 80 is absorbed in the imaging subject, and some of the remaining neutrons are absorbed in the $^{10}\text{B}_4\text{C}$ converter layer. When a
 81 ^{10}B nucleus absorbs a neutron, the reaction products, ^4He and ^7Li that are emitted head off in the opposite direction. One of
 82 them passes through the emulsion layer, creating a track of a few micrometers in length. Figure 1b shows a photograph of the
 83 developed detector. After the chemical development, grayscale images are obtained with submicrometer precision from the
 84 optical microscope, and silver grains become visible.

85 Imaging of the PSI Siemens star test pattern

86 Figure 2a shows a photograph of the Siemens star test pattern used in the experiments performed in this study. This pattern is
 87 designed by a group based at the Paul Scherrer Institute (PSI), Villigen, Switzerland. A prototype of the test pattern is described
 88 in Ref.³⁸. The pattern consists of 128 spokes in a circular area of 20 mm diameter and is made of a thin layer (in the order of 5
 89 μm) of gadolinium on a quartz wafer with a thickness of 0.7 mm. The space between the spokes becomes narrower towards the
 90 center of the circle. The innermost spoke has a period of 10 μm , which corresponds to 100 line pairs per millimeter. Then, the
 91 spatial resolution of an imaging device is assessed by how fine the intervals of the spokes can be resolved.

92 Figure 2b shows a photograph of the developed detector irradiated with the neutron beam through the pattern. The pattern
 93 transferred on the emulsion layer is visible to the naked eyes even before being observed under optical microscope. The dark
 94 regions correspond to sites where silver grains have been produced by the emitted ^4He or ^7Li during the neutron absorption
 95 events. Other regions correspond to sites where the neutrons are absorbed by gadolinium on the pattern, and neutron absorption
 96 events in the $^{10}\text{B}_4\text{C}$ layer are suppressed. Figure 2c shows a micrograph of the nuclear emulsion, which recorded the thinnest
 97 spokes near the center of the pattern. Because the innermost spokes having a period of 10 μm are clearly resolved, this result
 98 shows the ability of the fine-grained nuclear emulsion to achieve the spatial resolution of micrometer-scale or better.

99 Imaging of the gadolinium-based grating

100 The spatial resolution of the neutron imaging with the detector developed in the present work was investigated by using a
 101 grating made of gadolinium with a periodic structure of 9 μm , that is, 111 line pairs per millimeter. Figure 3a shows an image
 102 of the gadolinium-based grating formed on the silicon substrate. The grating was initially made for a Talbot–Lau interferometer
 103 for neutron phase imaging³⁹. Figure 3b shows a scanning electron microscopy (SEM) image of the grating produced by the
 104 same process as that used in the performed experiments. Figure 3c shows a SEM image of the cross-section of a gadolinium
 105 tooth and Figure 3d shows a schematic view of the gadolinium teeth. Gadolinium teeth with a width of approximately 5 μm

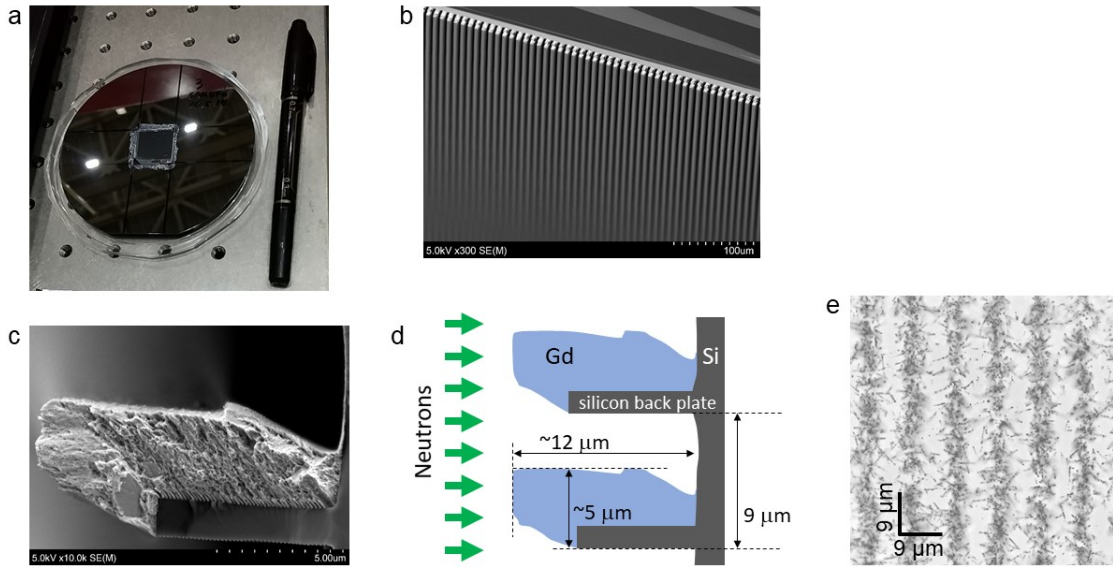


Figure 3. Neutron imaging of the gadolinium-based grating. **a** A picture of a gadolinium-based grating with dimensions of 20 mm × 20 mm. It was formed on a 525 μm-thick silicon substrate and mounted at the centre of a 525 μm-thick five-inch silicon wafer. **b** Image of the structure of the gadolinium teeth obtained by scanning electron microscopy (SEM). **c** SEM image of the cross-section of a single gadolinium tooth. **d** Schematic view of the gadolinium teeth. The direction of the irradiated neutrons was from left to right. A portion of the incident neutron is absorbed by the gadolinium, while the remnant neutrons pass through the empty spaces. **e** Optical micrograph of the neutron detector that recorded the tracks during neutron capture events through the grating. One side of this micrograph corresponds to 1024 pixels, which is equal to 56 μm.

106 and empty spaces of 4 μm were formed periodically. Each tooth was formed by depositing gadolinium from an oblique angle
 107 onto the ridge-like structures formed on the silicon substrate³⁹.

108 Figure 3e shows a micrograph of tracks recorded in the nuclear emulsion layer. The dimensions and number of pixels of
 109 this micrograph are 56 μm × 56 μm and 1024 pixels × 1024 pixels, respectively. The periodic structure with 9 μm is clearly
 110 visible.

111 Evaluation of the spatial resolution

We produced edge profiles from the obtained micrographs of the neutron detector and fitted the Gaussian error function to evaluate the edge rise. The error function is described by the following equation:

$$Error\ function(x) = \frac{A}{\sqrt{2\pi}\sigma} \int_0^x \exp\left(-\frac{(t-\mu)^2}{2\sigma^2}\right) dt + B. \quad (1)$$

112 where A is the amplitude, B is the base value, μ is the mean, and σ is the diffuseness of the edge.

113 Before the fitting process, we converted the grayscale micrograph into a binarised image, as shown in Figure 4a, using the
 114 image processing described in the Methods section. The coordinates are also shown in the figure. In the binarised image, the
 115 white and black pixels correspond to the areas where the silver grains are present and absent, respectively. Using the image, the
 116 number of the white pixels in the direction parallel to the grating (Y-direction) was calculated at a certain X-value with a range
 117 of bin sizes, as shown in Figure 4b. The length of the error bar for each point corresponds to the square root of the number of
 118 white pixels in each line. Then, we divided this graph into individual edge sections by detecting the positions of the peaks and
 119 valleys of the periodic structure. The green lines in Figure 4b represent the defined boundaries of each edge section. The falling
 120 and rising edges are treated separately in the subsequent analyses to distinguish between the two sides of the gadolinium tooth,
 121 that is, one with a silicon back plate and one without it, as shown in Figure 3d. These two sides correspond to the falling and
 122 rising edges, respectively. To exclude the incomplete stripes in the peripheral part of the micrograph and equalise the number
 123 of rising and falling edges, we defined pairs of adjacent rising and falling edges and used the paired edges in the subsequent

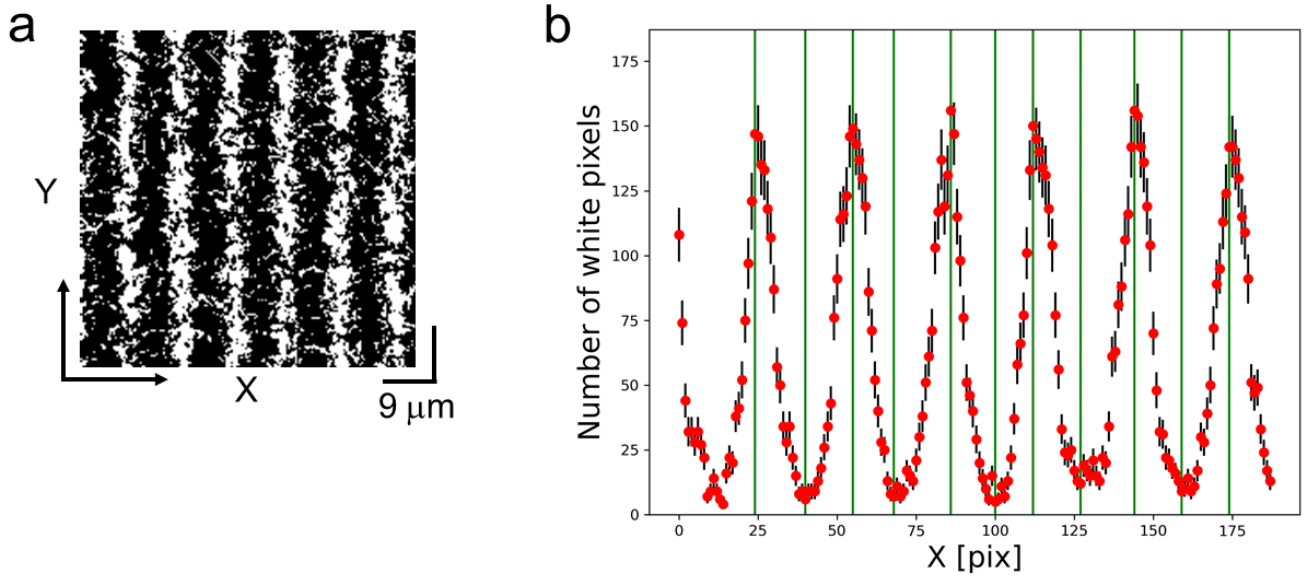


Figure 4. Data processing of neutron imaging of the gadolinium-based grating. **a** A resised and binarised micrograph of an optical micrograph of the neutron detector, as shown in Figure 3e. The dimensions of this micrograph were $56 \mu\text{m} \times 56 \mu\text{m}$. It was scaled down to $188 \text{ pixels} \times 188 \text{ pixels}$, such that the size of one pixel is equivalent to $0.3 \mu\text{m}$, which is the typical apparent diameter of a silver grain. Each white pixel corresponds to an area in which silver grains were present. **b** Number of white pixels along as a function of the X position. The length of each error bar corresponds to the square root of the number of white pixels. The green lines are the positions of the peaks and valleys, and the defined boundaries of individual edge sections. To equalise the number of rising and falling edges in the subsequent analysis, we only used the four pairs of rising and four falling edges in the region ($40 < X < 159$) from this data.

124 analysis. We applied this data processing to the obtained micrographs of 168 field-of-views, which correspond to an area of
 125 0.65 mm^2 .

126 Figure 5a,b shows the fitting for a rising edge and falling edge, respectively, using Eq. (1). The red dotted lines show
 127 the fitted error function curves. The fitting was conducted in the range between the maximum and minimum points in each
 128 cut section. A total of 709 rising and 709 falling edges were used in the analysis, and Figure 6 shows the distributions of the
 129 reduced χ^2 of the fitting.

130 Because the diffuseness distributions of the rising and falling edges are asymmetric with a tail to the right side, as shown in
 131 Figure 7, we employed a log-normal distribution described by the following equation:

$$\text{Log-normal distribution}(x) = \frac{A}{\sqrt{2\pi}\sigma_x} \exp\left(-\frac{(\ln x - \mu)^2}{2\sigma^2}\right). \quad (2)$$

132 where A is the amplitude factor, $\exp(\mu)$ is the median value, and σ is a parameter that correlates with the width of this
 133 distribution. The χ^2 divided by the number of degrees of freedom of the fitting for the rising and falling edges were $25.9 / 19$
 134 and $23.73 / 16$, respectively. The deduced median values of the diffuseness distributions of the rising and falling edges are 0.91
 135 ± 0.01 and $0.88 \pm 0.01 \mu\text{m}$, and their mean values are 0.96 ± 0.01 and $0.93 \pm 0.01 \mu\text{m}$, respectively. These values are less
 136 than $1 \mu\text{m}$, as shown in Figure 7.

137 Discussion

138 We evaluated the median values of the diffuseness for the rising and falling edges to be 0.91 ± 0.01 and $0.88 \pm 0.01 \mu\text{m}$,
 139 respectively. These values for the rising and falling edges are consistent within three standard deviations. Here, the shape of
 140 the gadolinium teeth is not a perfect rectangle because of the production process, as described in Ref.^{40,41}. Therefore, the
 141 analysis presented in this paper is an inclusive assessment that includes the effects of the resolution of the detector and the
 142 shape of the gadolinium tooth. However, because the median values of the diffuseness are less than $1 \mu\text{m}$, we have achieved a
 143 submicrometer spatial resolution using a fine-grained nuclear emulsion for neutron imaging. To the best of our knowledge, the
 144 achieved spatial resolution is the best among the neutron imaging devices reported to date.

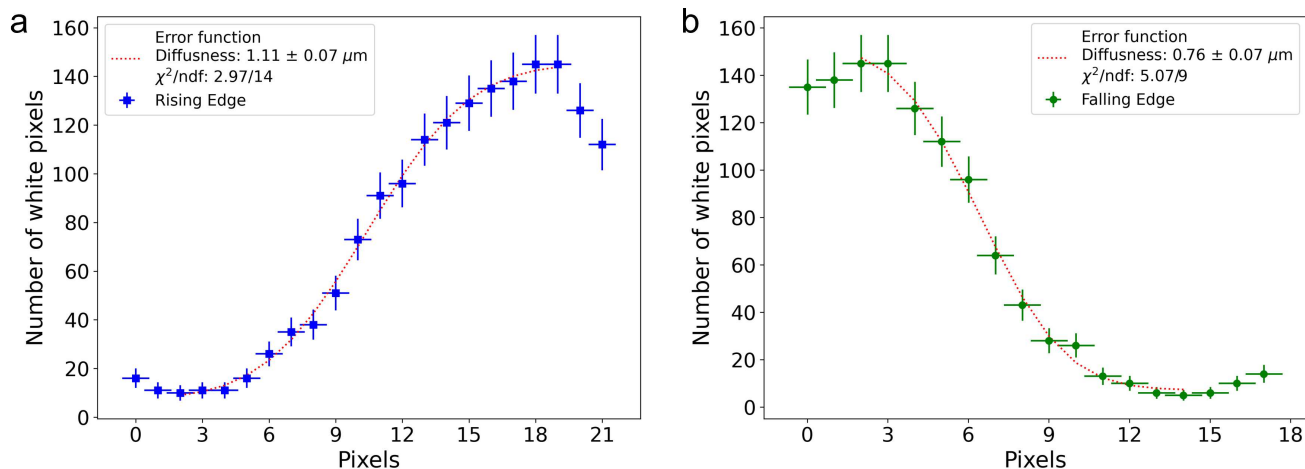


Figure 5. Examples of data points of the edges and their fitting with the Gaussian error function. Panels a and b show the rising and falling edges, respectively. The red dotted lines represent the curves obtained by the fitting. The fitting range is defined between the minimum and maximum points.

145 As demonstrated herein, precise neutron imaging using fine-grained nuclear emulsion will open a new avenue for non-
 146 destructive inspection to visualize the internal structure of advanced materials such as memory chips and fuel cells. For fuel
 147 cells, it is essential to visualize the water distribution during operation to improve its performance. Moreover, this technique
 148 can be used in the development of neutron optics elements such as gadolinium-based gratings. For instance, gadolinium-based
 149 gratings with micrometer-scale structures are used in neutron imaging with Talbot–Lau interferometry, and gratings with finer
 150 structures lead to a better wavelength resolution of Talbot–Lau imaging. The use of fine-grained nuclear emulsion detectors
 151 in the development of gratings can improve the resolution of interferometry techniques. Another potential application of
 152 precise neutron imaging is the inspection of test patterns for neutron imaging with a micrometer-scale structure. As the spatial
 153 resolution of neutron imaging approaches the micrometer scale, test patterns with micrometer-scale become important for
 154 evaluating imaging quality⁹. It is essential to observe such test patterns with neutron transmission, in addition to scanning
 155 electron microscopy and X-ray microscopy. Moreover, this technique could also be helpful in evaluating newly developed
 156 neutron imaging devices aiming to achieve a micrometer-scale spatial resolution. Neutron imaging may be conducted for a test
 157 pattern with a micrometer-scale structure using the nuclear emulsion and another developing neutron imaging device. The
 158 resolution of the developing device and the diffuseness caused by the beam divergence separately can be deduced by analysing
 159 and comparing the obtained images.

160 The fine-grained nuclear emulsion detector is lightweight, thin, small (even adjustable to sample objects with an area of
 161 approximately 100 cm^2), and can be set without an electrical power supply. Therefore, this detector can be added to existing
 162 imaging systems without major modifications and can be used as a complementary imaging device. Precise neutron imaging
 163 using fine-grained nuclear emulsion may provide new insights in a wide range of research fields and potential applications, for
 164 example, biology, geomechanics, and advanced materials such as semiconductor devices, batteries, and fuel cells.

165 Methods

166 Detector

167 The $^{10}\text{B}_4\text{C}$, NiC, and C layers were formed on a silicon substrate by an ion beam sputtering machine available at the Institute for
 168 Integrated Radiation and Nuclear Science of Kyoto University³⁷. The thickness of the $^{10}\text{B}_4\text{C}$ layer was adjusted by controlling
 169 the sputtering time, using the value of 1.25 nm/min of film growth speed measured in a preliminary experiment. The detection
 170 efficiency of neutrons with this $^{10}\text{B}_4\text{C}$ layer was measured to be approximately 0.4% for neutrons with a velocity of 2200 m/s .
 171 These three layers were formed on a 3-inch silicon substrate with a thickness of 0.4 mm . The emulsion layer was formed on a
 172 piece of substrate in a dark room by pouring and drying the fine-grained nuclear emulsion. Each detector was packed with a
 173 light- and moisture-proof laminated bag, which was composed of nylon, polyethylene, aluminum, polyethylene, and black
 174 polyethylene layers having thicknesses of $15 \mu\text{m}$, $13 \mu\text{m}$, $7 \mu\text{m}$, $13 \mu\text{m}$, and $35 \mu\text{m}$, respectively.

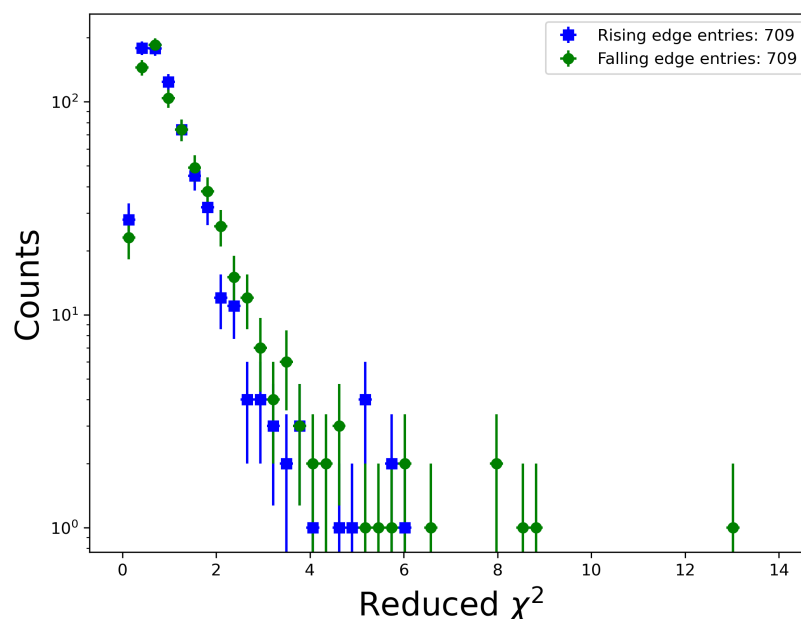


Figure 6. Distribution of reduced χ^2 values for the fitting with the error function. A total of 709 rising and 709 falling edges were used.

175 Beam exposure

176 We used the low-divergence beam branch⁴² of BL05 in the Materials and Life Science Experimental Facility (MLF) at the
 177 Japan Proton Accelerator Research Complex (J-PARC). This is one of the most suitable beam branches in the MLF for this
 178 experiment because it provides a reasonably intense neutron beam owing to a coupled neutron moderator.

179 For neutron imaging of the PSI Siemens star, the divergences of the beam in the horizontal and vertical directions were set
 180 to 0.3 mrad and 1.0 mrad, respectively. The typical beam power and the neutron flux during the experiment were 0.7 MW and
 181 10^5 n/cm²/s, respectively. The irradiation time was 9 h to accumulate approximately 10^4 tracks per (100 μm)². In contrast, for
 182 neutron imaging of the gadolinium-based grating, the beam divergence in the vertical direction was set to 10 mrad because the
 183 beam divergence parallel to the grating does not affect the blurring of the image. Then, the neutron flux was 2×10^6 n/cm²/s,
 184 and the neutron irradiation time was 2.8 h to accumulate approximately 2×10^4 tracks per (100 μm)².

185 Chemical development

186 After neutron irradiation, the chemical development of the detectors was conducted in a dark room. The development process
 187 involves immersing the detectors in the developing, stopping, and fixing solutions. The main agent of the developer was
 188 ascorbic acid, and the temperature was fixed to 20 °C. The immersion times in the developing, stopping, and fixing solutions
 189 were 5 min, 5 min, and 12 min, respectively. The detectors were then rinsed in tap water for 10 min and dried for 1 h.

190 Scanning of the neutron detector

191 A dedicated optical microscope with an epi-illumination system was used to scan the emulsion layer on a non-transparent
 192 silicon substrate. The light source of this system was a 1 W LED with a peak wavelength of 455 nm. The objective lens is
 193 an oil-immersion type with a magnification of 100x with a numerical aperture (NA) of 1.45 (Nikon Plan Apo). The depth of
 194 field was derived as $2 \times \lambda / \text{NA}^2 \simeq 0.43 \mu\text{m}$. The micrographs were acquired as 8-bit grayscale images with a complementary
 195 metal–oxide–semiconductor (CMOS) image sensor with 2048 pixels \times 2048 pixels (SENTECH CMB401PCL) at speeds
 196 of up to 160 frames per second. The length of one side of the field of view is approximately 112 μm , that is, a single pixel
 197 corresponds to 0.055 μm . We only use the central region of the micrograph (i.e., 1024 pixels \times 1024 pixels), because optical
 198 aberration in the periphery of the field of view reduces the quality of the image. Three independent stepping motors control the
 199 stage of the microscope along the two horizontal axes and the vertical axis. This microscope system acquires sequential images
 200 along the vertical axis with a pitch of 0.3 μm from the upper boundary to the lower boundary of the emulsion layer. The system
 201 shifts the field of view in the horizontal direction at a 50 μm pitch and scans the specified area.

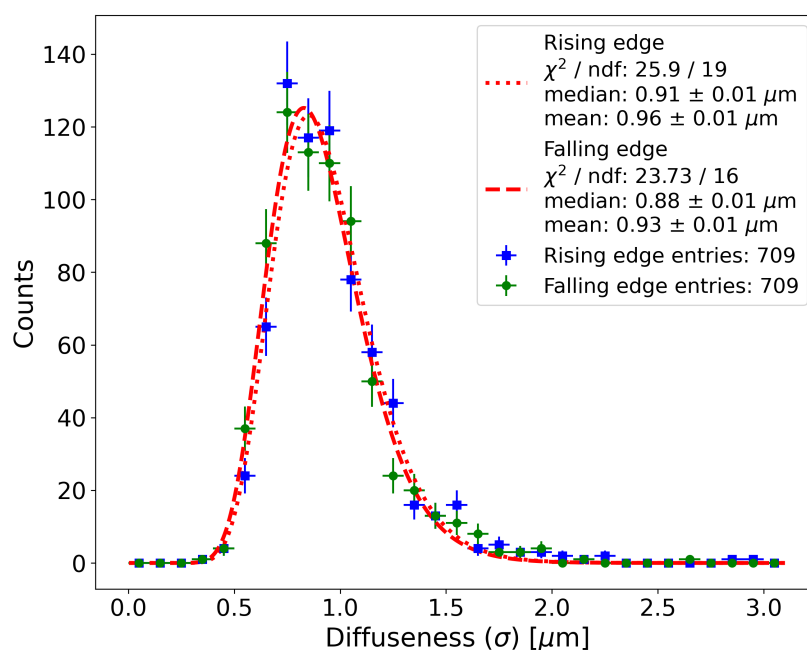


Figure 7. Distributions of the diffuseness and their fitting results. The blue and green marks represent the obtained diffuseness distributions for the rising and falling edges, respectively. The dotted and dashed red lines are the log-normal fit curves for the rising and falling edges, respectively.

202 Image processing

203 The following image processing sequence was carried out before evaluating the spatial resolution of the neutron imaging:
 204 creation of division images, resizing, and binarization. The images acquired by the optical microscope contain shades of dust
 205 on the image sensor and non-uniformity of brightness due to optical conditions. To remove them, the division images were
 206 created by the following process. We calculated the average brightness for each pixel and generated a mean image using a set of
 207 sequential tomographic images acquired at different depths of the focus plane. The image at the depth of the boundary between
 208 the sputtered C layer and the emulsion layer was selected. The brightness value of each image was divided by the brightness
 209 value of the corresponding pixel in the mean image. The division images were resized to 188 pixels \times 188 pixels such that
 210 the size of one pixel was equal to 0.3 μm , corresponding to the typical apparent diameter of the silver grain. Furthermore,
 211 we applied Otsu's binarization⁴³ to convert the grayscale images to binarised images by employing a non-parametric and
 212 unsupervised method, as shown in Figure 4a. Here, white and black pixels correspond to areas where the silver grains are
 213 present and absent, respectively.

214 Data availability

215 The data that support the findings of this study are available from the corresponding author upon reasonable request.

216 Code availability

217 Computer codes that support the findings of this study are available from the corresponding author upon reasonable request.

218 References

- 219 1. Strobl, M. *et al.* Topical review: Advances in neutron radiography and tomography. *JOURNAL OF PHYSICS D: APPLIED*
 220 *PHYSICS* **42**, 243001, DOI: <https://doi.org/10.1088/0022-3727/42/24/243001> (2009).
- 221 2. Hussey, D. S. & Jacobson, D. L. Applications of neutron imaging and future possibilities. *Neutron News* **26**, 19–22, DOI:
 222 <https://doi.org/10.1080/10448632.2015.1028273> (2015).
- 223 3. Lehmann, E. H., Boillat, P., Kaestner, A., Vontobel, P. & Mannes, D. Neutron imaging methods for the investigation of
 224 energy related materials. *EPJ Web Conf.* **104**, 01007, DOI: <https://doi.org/10.1051/epjconf/201510401007> (2015).

- 225 4. Kardjilov, N., Manke, I., Woracek, R., Hilger, A. & Banhart, J. Advances in neutron imaging. *Mater. Today* **21**, 652–672,
226 DOI: <https://doi.org/10.1016/j.mattod.2018.03.001> (2018).
- 227 5. Tengattini, A., Lenoir, N., Andò, E. & Viggiani, G. Neutron imaging for geomechanics: A review. *Geomech. for Energy*
228 *Environ.* **27**, 100206, DOI: <https://doi.org/10.1016/j.gete.2020.100206> (2021). Deformation Characteristics of Geomaterials
229 – selected papers for 7th International Symposium, IS-Glasgow2019.
- 230 6. Banhar, J. Advanced tomographic methods in materials research and engineering. (*Oxford: Oxf. Univ. Press.* DOI:
231 <https://doi.org/10.1093/acprof:oso/9780199213245.001.0001> ((ed) 2008).
- 232 7. Tremsin, A. *et al.* Improved efficiency of high resolution thermal and cold neutron imaging. *NUCL INSTRUM METH*
233 *PHYS RES A* **628**, 415–418, DOI: <https://doi.org/10.1016/j.nima.2010.07.014> (2011).
- 234 8. Hussey, D. *et al.* A new cold neutron imaging instrument at nist. *Phys. Procedia* **69**, 48–54, DOI: <https://doi.org/10.1016/j.phpro.2015.07.006> (2015).
235
- 236 9. Trtik, P. *et al.* Improving the spatial resolution of neutron imaging at paul scherrer institut – the neutron microscope project.
237 *Phys. Procedia* **69**, 169–176, DOI: <https://doi.org/10.1016/j.phpro.2015.07.024> (2015).
- 238 10. Trtik, P. & Lehmann, E. H. Progress in high-resolution neutron imaging at the paul scherrer institut - the neutron microscope
239 project. *J. Physics: Conf. Ser.* **746**, 012004, DOI: <https://doi.org/10.1088/1742-6596/746/1/012004> (2016).
- 240 11. Bingham, P., Santos-Villalobos, H., Lavrik, N., Gregor, J. & Bilheux, H. Magnified neutron radiography with coded
241 sources. *Phys. Procedia* **69**, 218–226, DOI: <https://doi.org/10.1016/j.phpro.2015.07.031> (2015).
- 242 12. Morgano, M. *et al.* Unlocking high spatial resolution in neutron imaging through an add-on fibre optics taper. *Opt. Express*
243 **26**, 1809–1816, DOI: <https://doi.org/10.1364/OE.26.001809> (2018).
- 244 13. Trtik, P. *et al.* PSI ‘Neutron Microscope’ at ILL-D50 Beamline – First Results. *Mater. Res. Proc.* **15**, 23–28, DOI:
245 <https://doi.org/10.21741/9781644900574-4> (2020).
- 246 14. Woracek, R. *et al.* Spatially resolved time-of-flight neutron imaging using a scintillator cmos-camera detector with khz
247 time resolution. *Opt. Express* **27**, 26218–26228, DOI: <https://doi.org/10.1364/OE.27.026218> (2019).
- 248 15. Hussey, D. S., LaManna, J. M., Baltic, E. & Jacobson, D. L. Neutron imaging detector with 2 μm spatial resolution based
249 on event reconstruction of neutron capture in gadolinium oxysulfide scintillators. *Nucl. Instruments Methods Phys. Res.*
250 *Sect. A: Accel. Spectrometers, Detect. Assoc. Equip.* **866**, 9–12, DOI: <https://doi.org/10.1016/j.nima.2017.05.035> (2017).
- 251 16. Lattes, C. M. G., Occhialinidr., G. P. S. & Powell, C. F. Observations on the tracks of slow mesons in photographic
252 emulsions*. *Nature* **160**, 453–456, DOI: <https://doi.org/10.1038/160453a0> (1947).
- 253 17. Danysz, M. & Pniewski, J. Delayed disintegration of a heavy nuclear fragment: I. *The London, Edinburgh, Dublin Philos.*
254 *Mag. J. Sci.* **44**, 348–350, DOI: <https://doi.org/10.1080/14786440308520318> (1953).
- 255 18. Davis, D. 50 years of hypernuclear physics: I. the early experiments. *Nucl. Phys. A* **754**, 3–13, DOI: <https://doi.org/10.1016/j.nuclphysa.2005.01.002> (2005). Proceedings of the Eighth International Conference on Hypernuclear and Strange
256 Particle Physics.
257
- 258 19. Niu, K., Mikumo, E. & Maeda, Y. A Possible Decay in Flight of a New Type Particle. *Prog. Theor. Phys.* **46**, 1644–1646,
259 DOI: <https://doi.org/10.1143/PTP.46.1644> (1971). <https://academic.oup.com/ptp/article-pdf/46/5/1644/5271903/46-5-1644.pdf>.
260
- 261 20. Danysz, M. *et al.* The identification of a double hyperfragment. *Nucl. Phys.* **49**, 121–132, DOI: [https://doi.org/10.1016/0029-5582\(63\)90080-4](https://doi.org/10.1016/0029-5582(63)90080-4) (1963).
262
- 263 21. Yoshimoto, M., Nakano, T., Komatani, R. & Kawahara, H. Hyper-track selector nuclear emulsion readout system aimed at
264 scanning an area of one thousand square meters. *Prog. Theor. Exp. Phys.* **2017**, DOI: <https://doi.org/10.1093/ptep/ptx131>
265 (2017).
- 266 22. Saito, T. R. *et al.* New directions in hypernuclear physics. *Nat. Rev. Phys.* DOI: <https://doi.org/10.1038/s42254-021-00371-w> (2021).
267
- 268 23. Kodama, K. *et al.* Final tau-neutrino results from the DONuT experiment. *Phys. Rev. D* **78**, 052002, DOI: <https://doi.org/10.1103/PhysRevD.78.052002> (2008).
269
- 270 24. OPERA Collaboration *et al.* Observation of tau neutrino appearance in the CNGS beam with the OPERA experiment.
271 *Prog. Theor. Exp. Phys.* **2014**, DOI: <https://doi.org/10.1093/ptep/ptu132> (2014). 101C01, <https://academic.oup.com/ptep/article-pdf/2014/10/101C01/4414189/ptu132.pdf>.
272

- 273 25. Hiyama, E. & Nakazawa, K. Structure of S=-2 Hypernuclei and Hyperon-Hyperon Interactions. *Annu. Rev. Nucl. Part. Sci.*
274 **68**, 131–159, DOI: [10.1146/annurev-nucl-101917-021108](https://doi.org/10.1146/annurev-nucl-101917-021108) (2018). <https://doi.org/10.1146/annurev-nucl-101917-021108>.
- 275 26. Ekawa, H. *et al.* Observation of a Be double-Lambda hypernucleus in the J-PARC E07 experiment. *Prog. Theor. Exp.*
276 *Phys.* **2019**, DOI: <https://doi.org/10.1093/ptep/pty149> (2019). 021D02, [https://academic.oup.com/ptep/article-pdf/2019/2/](https://academic.oup.com/ptep/article-pdf/2019/2/021D02/27970468/pty149.pdf)
277 [021D02/27970468/pty149.pdf](https://academic.oup.com/ptep/article-pdf/2019/2/021D02/27970468/pty149.pdf).
- 278 27. Hayakawa, S. H. *et al.* Observation of Coulomb-Assisted Nuclear Bound State of $\Xi^- - ^{14}\text{N}$ System. *Phys. Rev. Lett.* **126**,
279 062501, DOI: <https://doi.org/10.1103/PhysRevLett.126.062501> (2021).
- 280 28. Yoshimoto, M. *et al.* First observation of a nuclear s-state of a Ξ hypernucleus, $^{15}_{\Xi}\text{C}$. *Prog. Theor. Exp. Phys.* **2021**,
281 DOI: <https://doi.org/10.1093/ptep/ptab073> (2021). 073D02, [https://academic.oup.com/ptep/article-pdf/2021/7/073D02/](https://academic.oup.com/ptep/article-pdf/2021/7/073D02/39257193/ptab073.pdf)
282 [39257193/ptab073.pdf](https://academic.oup.com/ptep/article-pdf/2021/7/073D02/39257193/ptab073.pdf).
- 283 29. Tanaka, H. K. *et al.* High resolution imaging in the inhomogeneous crust with cosmic-ray muon radiography: The
284 density structure below the volcanic crater floor of Mt. Asama, Japan. *Earth Planet. Sci. Lett.* **263**, 104–113, DOI:
285 <https://doi.org/10.1016/j.epsl.2007.09.001> (2007).
- 286 30. Morishima, K. *et al.* Discovery of a big void in khufu's pyramid by observation of cosmic-ray muons. *Nature* **552**, 386–390,
287 DOI: <https://doi.org/10.1038/nature24647> (2017).
- 288 31. Naka, T. *et al.* Fine grained nuclear emulsion for higher resolution tracking detector. *Nucl. Instruments Methods Phys.*
289 *Res. Sect. A: Accel. Spectrometers, Detect. Assoc. Equip.* **718**, 519–521, DOI: <https://doi.org/10.1016/j.nima.2012.11.106>
290 (2013).
- 291 32. Asada, T., Naka, T., Kuwabara, K.-i. & Yoshimoto, M. The development of a super-fine-grained nuclear emulsion. *Prog.*
292 *Theor. Exp. Phys.* **2017**, DOI: <https://doi.org/10.1093/ptep/ptx076> (2017).
- 293 33. Alexandrov, A. *et al.* Intrinsic neutron background of nuclear emulsions for directional Dark Matter searches. *Astropart.*
294 *Phys.* **80**, 16–21, DOI: <https://doi.org/10.1016/j.astropartphys.2016.03.003> (2016).
- 295 34. Shiraishi, T. *et al.* Development of a new tracking detector with fine-grained nuclear emulsion for sub-MeV neutron
296 measurement. *Prog. Theor. Exp. Phys.* **2021**, DOI: <https://doi.org/10.1093/ptep/ptab030> (2021). 043H01, [https://academic.](https://academic.oup.com/ptep/article-pdf/2021/4/043H01/37807850/ptab030.pdf)
297 [oup.com/ptep/article-pdf/2021/4/043H01/37807850/ptab030.pdf](https://academic.oup.com/ptep/article-pdf/2021/4/043H01/37807850/ptab030.pdf).
- 298 35. Naganawa, N. *et al.* A cold/ultracold neutron detector using fine-grained nuclear emulsion with spatial resolution less than
299 100 nm. *The Eur. Phys. J. C* **78**, 959, DOI: <https://doi.org/10.1140/epjc/s10052-018-6395-7> (2018).
- 300 36. Hirota, K. *et al.* Neutron Imaging Using a Fine-Grained Nuclear Emulsion. *J. Imaging* **7**, DOI: [https://doi.org/10.3390/](https://doi.org/10.3390/jimaging7010004)
301 [jimaging7010004](https://doi.org/10.3390/jimaging7010004) (2021).
- 302 37. Hino, M. *et al.* The ion beam sputtering facility at KURRI: Coatings for advanced neutron optical devices. *Nucl. Instruments*
303 *Methods Phys. Res. Sect. A: Accel. Spectrometers, Detect. Assoc. Equip.* **797**, 265–270, DOI: [https://doi.org/10.1016/j.](https://doi.org/10.1016/j.nima.2015.06.046)
304 [nima.2015.06.046](https://doi.org/10.1016/j.nima.2015.06.046) (2015).
- 305 38. Grünzweig, C., Frei, G., Lehmann, E., Kühne, G. & David, C. Highly absorbing gadolinium test device to characterize the
306 performance of neutron imaging detector systems. *Rev. Sci. Instruments* **053708**, DOI: <https://doi.org/10.1063/1.2736892>
307 (2007).
- 308 39. Seki, Y. *et al.* Experimental Evaluation of Neutron Absorption Grating Fabricated by Oblique Evaporation of Gadolinium
309 for Phase Imaging. *Phys. Procedia* **88**, 217–223, DOI: <https://doi.org/10.1016/j.phpro.2017.06.030> (2017).
- 310 40. Samoto, T., Takano, H. & Momose, A. Gadolinium oblique evaporation approach to make large scale neutron absorption
311 gratings for phase imaging. *Jpn. J. Appl. Phys.* **58**, SDDF12, DOI: <https://doi.org/10.7567/1347-4065/ab138d> (2019).
- 312 41. Samoto, T., Takano, H. & Momose, A. Evaluation of obliquely evaporated gadolinium gratings for neutron interferometry
313 by X-ray microtomography. *Mater. Sci. Semicond. Process.* **92**, 91–95, DOI: <https://doi.org/10.1016/j.mssp.2018.05.038>
314 (2019). Material processing of optical devices and their applications.
- 315 42. Mishima, K. *et al.* Design of neutron beamline for fundamental physics at J-PARC BL05. *Nucl. Instruments Methods Phys.*
316 *Res. Sect. A: Accel. Spectrometers, Detect. Assoc. Equip.* **600**, 342–345, DOI: <https://doi.org/10.1016/j.nima.2008.11.087>
317 (2009).
- 318 43. Otsu, N. A Threshold Selection Method from Gray-Level Histograms. *IEEE Transactions on Syst. Man, Cybern.* **9**, 62–66,
319 DOI: <https://doi.org/10.1109/TSMC.1979.4310076> (1979).

320 Acknowledgements

321 The neutron experiment at the Materials and Life Science Experimental Facility of the J-PARC was performed under user
322 programs (Proposal No. 2020B0223). The preliminary experiment on the detector was performed at the Research Reactor
323 Institute, Kyoto University (Experiment No. R2138). J. Y. was supported by JSPS KAKENHI Grant Number JP18H05403
324 (Grant-in-Aid for Scientific Research on Innovative Areas 6005). The authors thank Takenao Shinohara of J-PARC and
325 Yoshichika Seki of Osaka electro-communication University for lending the Siemens star test pattern and the grating, and
326 Atsushi Momose and Tetsuo Samoto of Tohoku University for providing the SEM images shown in figure 3 and for the
327 discussions related to the grating. The authors also thank Atsuhiko Umemoto and Ryuta Kobayashi from Nagoya University for
328 their technical support in using the optical microscope. The authors would like to thank Yukiko Kurakata of the High Energy
329 Nuclear Physics Laboratory at RIKEN for providing administrative support for the entire project.

330 Author contributions statement

331 K.H, T.R.S proposed this study, and T.R.S managed the project. A.M, J.Y, M.H, N.M, N.N produced the neutron detectors.
332 A.M, J.Y, K.H., M.H, G.I, K.M, M.N. performed the experiments. A.M, J.Y, N.N performed observation and scanning of the
333 detectors. A.M, J.Y, A.K performed the analysis. A.M, J.Y, H.E, M.H, K.H, G.I, A.K, M.K, N.M, K.M, J.U.N, M.N, N.N,
334 T.R.S contributed in writing the manuscript. All authors contributed to finalizing the manuscript and approved the final draft.